Journal of
*Manufacturing and Materials Processing*

MDPI

*Article*

# Machine-Learning-Based Thermal Conductivity Prediction for Additively Manufactured Alloys

**Uttam Bhandari [1], Yehong Chen [1], Huan Ding [1], Congyuan Zeng [2], Selami Emanet [1], Paul R. Gradl [3] and Shengmin Guo [1,*]**

[1] Department of Mechanical & Industrial Engineering, Louisiana State University, Baton Rouge, LA 70803, USA
[2] Department of Mechanical Engineering, Southern University and A&M College, Baton Rouge, LA 70807, USA
[3] NASA/Marshall Space Flight Center, Huntsville, AL 35812, USA
* Correspondence: sguo2@lsu.edu

**Abstract:** Thermal conductivity (TC) is greatly influenced by the working temperature, microstructures, thermal processing (heat treatment) history and the composition of alloys. Due to computational costs and lengthy experimental procedures, obtaining the thermal conductivity for novel alloys, particularly parts made with additive manufacturing, is difficult and it is almost impossible to optimize the compositional space for an absolute targeted value of thermal conductivity. To address these difficulties, a machine learning method is explored to predict the TC of additive manufactured alloys. To accomplish this, an extensive thermal conductivity dataset for additively manufactured alloys was generated for several AM alloy families (nickel, copper, iron, cobalt-based) over various temperatures (300–1273 K). This unique dataset was used in training and validating machine learning models. Among the five different regression machine learning models trained with the dataset, extreme gradient boosting performs the best as compared with other models with an $R^2$ score of 0.99. Furthermore, the accuracy of this model was tested using Inconel 718 and GRCop-42 fabricated with laser powder bed fusion-based additive manufacture, which have never been observed by the extreme gradient boosting model, and a good match between the experimental results and machine learning prediction was observed. The average mean error in predicting the thermal conductivity of Inconel 718 and GRCop-42 at different temperatures was 3.9% and 2.08%, respectively. This paper demonstrates that the thermal conductivity of novel AM alloys could be predicted quickly based on the dataset and the ML model.

**Keywords:** thermal conductivity; additive manufacturing; machine learning; Bayesian optimization



**Citation:** Bhandari, U.; Chen, Y.; Ding, H.; Zeng, C.; Emanet, S.; Gradl, P.R.; Guo, S. Machine-Learning-Based Thermal Conductivity Prediction for Additively Manufactured Alloys. *J. Manuf. Mater. Process.* **2023**, *7*, 160. https://doi.org/10.3390/jmmp7050160

Academic Editors: Azadeh Haghighi, Prahalada Rao and Yunbo Zhang

Received: 20 July 2023
Revised: 22 August 2023
Accepted: 30 August 2023
Published: 3 September 2023



## 1. Introduction

Material selection for an end-use application is critical to ensure meeting various mechanical and thermophysical properties required. Each of the mechanical and thermophysical properties must be properly balanced based on the behavior under the expected operating conditions and environment. One crucial thermophysical property for various applications is thermal conductivity (TC). The temperature-sensitive TC values are a critical material parameter for heat transfer applications used in various applications including 5G communication technologies [1], cooling components of a computer [2], propulsion systems such as aircraft and rocket engines [3,4] industrial heat exchangers for power, energy, and processing [5] electronic and semiconductor devices [6]. Depending upon the end-use application, different types of materials with varying TC values are required. For example, mechanically stable materials with a low thermal conductivity are needed for coating the blades of gas turbine engines to improve power and efficiency at high temperatures [7]. Similarly, electronic devices require high TC materials to dissipate the generated heat [8]. However, due to the lack of design tools, it is extremely difficult to design a new material, such as a new alloy, with a targeted set of TC values. So, it is

necessary to choose and understand the right materials with desired thermal conductivity to dissipate the heat according to the requirements of the application in order to achieve the greatest performance.

Both first-principles and molecular dynamics (MD) calculations are the proven methods for calculating the lattice thermal conductivity of metals, semiconductors, binary alloys, and compounds [9–17]. However, these calculations remain challenging for the system of multicomponent alloys due to the complex structure and disorder phases that arise from the addition of multiple elements. For examples, to perform first-principle calculation of alloys, constructing models for simulation is difficult due to the complex chemical interaction that comes from the involvement of many principle elements [18]. Similarly, it is required to develop force field to perform MD simulations. Such force field is not readily available for novel alloys and constructing the force field is extremely challenging since alloys possess metastable phases depending upon methods of fabrications and processing [19]. Performing thermal properties calculation using first principles and MD simulation can easily consume more than 1,000,000 computer hours [16,20]. Therefore, high computational costs and the unavailability of force potential make even more difficult to predict the thermal properties of novel alloys as they have many principal elements. So far, experimental trial and error approach is the only feasible method to identify the TC of novel alloys. However, the screening process requires iterations and extensive testing which is lengthy and costly. To overcome the limitations of simulations and experimentally based material design approaches, machine learning (ML) is attempted in this study to predict TC for alloys. ML-based predictions can use a full or partial traditional dataset and allow for the opportunity to significantly lower costs [21–24]. Previously, many ML methods have been utilized to predict the lattice TC of materials, for example, Chen et al. [25] applied the Gaussian regression ML model to predict the lattice TC of organic compounds. The random forest regression model was applied by the Russlan group [26] to predict the lattice TC of crystals. Many researchers applied ML methods to predict lattice TC of graphene [27], metal oxides [28], half-heusler compounds [29], and polymers [30] with acceptable model performances. For training machine learning models, large amounts of data are often needed to obtain more accurate predictions. It is necessary to evaluate and identify suitable ML models, which do not require large training data for better accuracy. Nonetheless, there are no ML calculations on the TC of metal alloys with multicomponent elements particularly for additively manufactured materials.

In this work, machine learning methods were implemented and trained using collected experimental data to predict the TC of multicomponent alloys fabricated with AM methods. This ML method can quickly learn from the dataset and provide an accurate prediction with less cost and stress as compared to experimental and simulation methods. Figure 1 shows the prediction model used in ML for predicting thermal conductivity. The ML models are trained with the training set of data during the learning process. After the training, test data is supplied in each model for TC prediction. Five different machine learning models have been tested with the dataset and the best model was identified. It is found that extreme gradient boosting (XGB) regression performs better than other models and it predicts the TC of testing alloys accurately. A more detailed explanation of the experimental setup and ML model performance is provided in the Methods section.

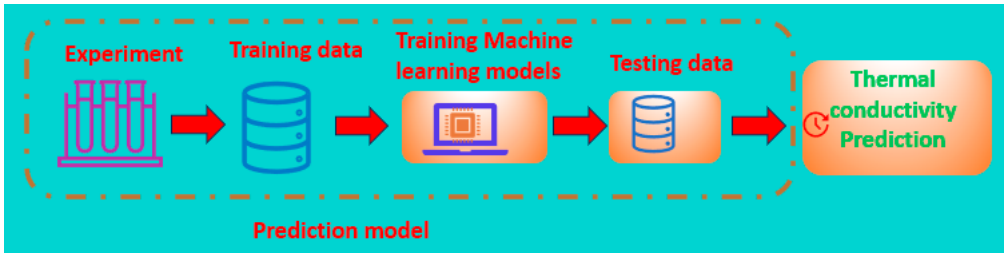


**Figure 1.** The ML framework for predicting thermal conductivity.

## 2. Machine Learning Methods

### 2.1. Establishment of an Alloy TC Database

A large set of samples were built using AM processes, appropriate heat treatments were completed, and the TC was measured across various nickel, copper, iron, and cobalt-based alloys. This dataset was funded by NASA and used as the starting dataset to train the ML model. Cylindrical-shaped alloy samples were fabricated with either laser powder bed fusion (L-PBF) or laser powder direct energy deposition (LP-DED) additive manufacturing processes. The AM samples were typically 13 mm in diameter with various length. Heat treatments, including stress relief, hot isostatic pressing (HIP), and the appropriate solution or aging were performed on the samples to tune microstructures and consequently performance [31,32]. A few select wrought samples were also included in the dataset to provide a comparison of the AM and wrought counterparts during the initial measurements of TC. The various types of alloy samples and the corresponding heat treatment cycle are listed in Table 1 [33]. According to this table, the final steps of the heat treatment procedures were either HIP or solution annealing via fast cooling (quenching or air cooling). HIP typically features a slow cooling rate, for example, several °C/min [34–36], which is around two orders of magnitude slower than the air-cooling rate [37], and more than three orders of magnitude slower than quenching [38]. Therefore, in this study, it is assumed that after the HIP treatment, phases at room temperature were retained, while after both air cooling and quenching, phases, and their compositions at the temperature where air cooling and quenching started were kept. Furthermore, during the thermophysical test, there is a significant temperature increase in material (up to 1000 °C) and phase transformation could potentially occur. However, this study aimed to emphasize a fundamental aspect of the machine learning model's design. While it is true that phase transitions could lead to changes in local element compositions, the current model operates on a different principle, which was specifically designed to capture the relationship between composition, thermal conductivity, and temperature, independent of the intricate phase change phenomena. Therefore, phase change during thermophysical test process was not specifically considered in this ML based study.

**Table 1.** List of the samples and the corresponding heat treatment information [33].

| Alloy | Process | Heat Treatment Procedures [a] |
|---|---|---|
| GRCop-42 | L-PBF | HIP [b] |
| GRCop-84 | L-PBF | HIP [b] |
| C-18150 | L-PBF | Sol (1000 °C for 9 h) |
| Inconel 625 | L-PBF | SR (1066 °C for 90 min) + HIP [b] + Sol (1177 °C for 60 min, quench) |
| Inconel 625 | LP-DED | SR (1066 °C for 90 min) + HIP [b] + Sol (1177 °C for 60 min, quench) |
| Inconel 625 | Wrought | Anneal (1010 °C for 60 min), quench |
| Inconel 718 | L-PBF | SR (1066 °C for 90 min) + HIP [b] + Sol (1066 °C for 60 min, quench) + Age (760 °C for 10 h, cool to 649 °C hold until total aging time of 20 h) |
| Inconel 939 | L-PBF | SR (1066 °C for 90 min) + HIP [b] + Sol (1090 °C for 4 h, quench) + Age (1000 °C for 6 h, quench + 800 °C for 4 h, air cooling) |
| Hastelloy X | L-PBF | SR (1066 °C for 90 min) + HIP [b] + Sol (1177 °C for 180 min, quench) |
| Hastelloy X | LP-DED | SR (1066 °C for 90 min) + HIP [b] + Sol (1177 °C for 180 min, quench) |
| Hastelloy X | Wrought | Hot rolled, anneal (1177 °C for 20 min), water quench |
| Haynes 230 | L-PBF | SR (1066 °C for 90 min) + HIP [b] + Sol (1177 °C for 60 min, quench) |
| Haynes 230 | LP-DED | SR (1066 °C for 90 min) + HIP [b] + Sol (1177 °C for 60 min, quench) |
| Haynes 230 | Wrought | Hot rolled, Sol (1204 °C for 30 min), quench |
| Haynes 282 | L-PBF | SR (1066 °C for 90 min) + HIP [b] + Sol (1135 °C for 60 min, quench) + Age (1010 °C for 120 min, cool to 788 °C hold until total aging time of 10 h, quench) |
| SS 316L | LP-DED | SR (899 °C for 120 min) + HIP [b] + Sol (1100 °C for 120 min, quench) |

**Table 1.** *Cont.*

| Alloy | Process | Heat Treatment Procedures [a] |
|---|---|---|
| 15-5, H1150 | LP-DED | SR (649 °C for 60 min) + HIP [b] + Sol (1050 °C for 60 min, air cool) + Age (621 °C for 60 min, air cool) |
| 17-4, H1150 | LP-DED | SR (649 °C for 60 min) + HIP [b] + Sol (1050 °C for 60 min, air cool) + Age (621 °C for 60 min, air cool) |
| NASA HR-1 | LP-DED 350W | SR (1066 °C for 90 min) + HIP [b] + Sol (1066 °C for 60 min, quench) + Age (691 °C for 16 h, cool to 621 °C hold until total aging time of 32 h) |
| JBK-75 | LP-DED | SR (982 °C for 90 min) + HIP [b] + Sol (982 °C for 60 min, quench) + Age (718 °C for 16 h) |
| CoCr | LP-DED | SR (1052 °C for 120 min) + HIP [b] + Sol (1100 °C for 120 min, quench) + Age (802 °C for 25 h, quench; 1000 °C for 60 min, quench) |

[a] Detailed heat treatment procedures should be verified; general procedures are only provided; [b] Hot Isostatic Pressing (HIP) Per ASTM 3301-18a; SR = Stress relief, slow cooling; Sol = Solution/Annealing; Age = Aging.

Three cylindrical disc samples for each alloy condition with the size of 12.55 mm in diameter and 2.5 mm in thickness were machined with wire electrical discharge machine (EDM) for the repeatability and credibility of the characterization testing. Prior to the tests, the sample surfaces were grinded using SiC paper with a grit size of 600 mesh. After the testing, the disk samples were rinsed in acetone, ethanol, and distilled water sequentially for 10 min each, followed by air-drying. The room-temperature densities of the alloys were measured with the Archimedes principle. Before the thermal property tests, the disk samples were sprayed with thin graphite coating for uniform surface conditions. A Netzsch LFA 467 HT HyperFlash®®-light flash apparatus was used to measure the thermal diffusivity values of the samples up to 1000 °C, with the calculated specific heat values of the samples by referring to the standard samples. Thermal conductivity of the alloy samples at different test temperatures can be described by the following equation:

$$K(T) = \alpha(T) \cdot C_p(T) \cdot \rho(T) \quad (1)$$

where $K(T)$, $\alpha(T)$, $C_p(T)$, and $\rho(T)$ are temperature-dependent thermal conductivity, thermal diffusivity, specific heat and density of the samples. Coefficients of thermal expansion were evaluated using a Netzsch DIL402SE dilatometer. Assume that after heat treatments, the alloy samples are isotropic, linear and volumetric thermal expansion data can be estimated, which can be used to modify density and thermal diffusivity data above room temperature. A more detailed description of the thermal property test procedures and results can be found in the authors' previous studies [33,39]. A total of 294 instances of TC from the various AM alloy samples (and a few wrought) were collected from the experiments. With all of the above tests and calculations, thermal conductivity of all the alloy samples is listed in Table 2. Furthermore, new TC data were collected on copper alloy GRCop-42 and GRCop-82 samples, Table 2. The GRCop alloy data provide the comparison among samples manufactured by different venders with different L-PBF AM systems and powder lots to determine the likely variability in thermophysical properties among the commercial vendor supply chain. As the goal of this paper is to develop machine learning models and make predictions based on alloy compositions, detailed GRCop-42 and GRCop-84 data with unique compositions are included in Table 3.

**Table 2.** Thermal conductivity data (W/(mK)) of the alloy samples over the test temperatures.

| Thermal Conductivity (W/(mK)) at Different Testing Temperatures (°C) | | | | | | | | | | | | |
|---|---|---|---|---|---|---|---|---|---|---|---|---|
| alloy | Process | 25 | 100 | 200 | 300 | 400 | 500 | 600 | 700 | 800 | 900 | 1000 |
| GRCop-42 | L-PBF | 327.5 | 328.7 | 329.4 | 328.4 | 325 | 322.1 | 316.9 | 305.8 | - | - | - |
| GRCop-84 | L-PBF | 286.4 | 285.5 | 286 | 285 | 282.5 | 279.8 | 274.6 | 265.9 | - | - | - |
| C-18150 | L-PBF | 271.2 | 284.4 | 297.8 | 305.4 | 308.9 | 322.9 | 324.4 | 314.3 | 299.7 | 281.7 | 252.4 |
| Inconel 625 | L-PBF | 10.3 | 11.7 | 13.9 | 16.6 | 19.5 | 18.7 | 20.6 | 23 | 23 | 24.6 | 25.6 |
| Inconel 625 | LP-DED | 10.6 | 12.1 | 14.4 | 17.2 | 20.2 | 19.2 | 21 | 23.4 | 23 | 25.1 | 26.4 |
| Inconel 625 | Wrought | 10.4 | 11.6 | 13.5 | 16.5 | 19.4 | 18.6 | 20.6 | 22.9 | 23 | 24.9 | 25.4 |
| Inconel 939 | L-PBF | 10.4 | 11.8 | 13.5 | 16 | 18.4 | 18.3 | 20.3 | 21.8 | 23.2 | 25 | 25.6 |
| Inconel 718 | L-PBF | 10.3 | 11.7 | 13.8 | 16.3 | 19.1 | 18.3 | 19.5 | 24.9 | 25.4 | 24.0 | 25.2 |
| Hastelloy X | L-PBF | 11.1 | 12.8 | 15.3 | 17.9 | 21 | 20.6 | 23.7 | 26.3 | 29.5 | 28.8 | 29.4 |
| Hastelloy X | LP-DED | 10.5 | 12.1 | 14.5 | 17.1 | 19.9 | 19.5 | 22.4 | 24.8 | 28.7 | 27 | 27.9 |
| Hastelloy X | Wrought | 10.6 | 12.2 | 14.6 | 17.2 | 20.2 | 19.7 | 22.5 | 24.8 | 27.9 | 27.2 | 27.6 |
| Haynes 230 | L-PBF | 8.8 | 10.2 | 12.4 | 15 | 17.7 | 17.2 | 19 | 21.4 | 21.9 | 23.8 | 25.2 |
| Haynes 230 | LP-DED | 9.2 | 10.6 | 12.8 | 15.5 | 18.5 | 17.8 | 19.6 | 22 | 22.1 | 24.4 | 25.7 |
| Haynes 230 | Wrought | 9.1 | 10.5 | 12.8 | 15.5 | 18.4 | 17.8 | 19.5 | 21.7 | 22.6 | 24.6 | 26.3 |
| Haynes 282 | L-PBF | 10.9 | 12.3 | 14.4 | 16.8 | 19.6 | 19.1 | 20.9 | 23.3 | 23.4 | 25.2 | 26 |
| SS 316L | LP-DED | 13.3 | 14.9 | 17.2 | 19.5 | 22.1 | 22.6 | 28.9 | 31.7 | 42 | 32.4 | 31.4 |
| 15-5, H1150 | LP-DED | 16.1 | 17.7 | 19.6 | 21.2 | 22.6 | 21.9 | 24 | 31.5 | 44.8 | 33.7 | 32 |
| 17-4, H1150 | LP-DED | 15.2 | 16.7 | 18.5 | 20.1 | 21.6 | 21 | 22.4 | 30.6 | 43.6 | 32.8 | 31.3 |
| NASA HR-1 | LP-DED | 11.1 | 13 | 15.8 | 18.3 | 20.4 | 19.7 | 22.5 | 24.8 | 22.6 | 23.6 | 24.5 |
| JBK-75 | LP-DED | 12.3 | 13.9 | 16.2 | 18.8 | 21.5 | 21.4 | 26.3 | 28.8 | 36 | 29.3 | 29.2 |
| CoCr | LP-DED | 12 | 13.5 | 15.6 | 17.7 | 19.7 | 21.4 | 23.7 | 26 | 28.5 | 31.2 | 34.4 |
| GRCop-42-1 | L-PBF | 316.3 | 312.5 | 318.0 | 315.4 | 310.9 | 305.7 | 298.8 | 288.5 | - | - | - |
| GRCop-42-2 | L-PBF | 320.5 | 318.2 | 317.2 | 314.7 | 310.3 | 305.5 | 299.9 | 289.8 | - | - | - |
| GRCop-42-3 | L-PBF | 325.3 | 331.3 | 330.3 | 327.8 | 323.5 | 318.4 | 312.3 | 302.3 | - | - | - |
| GRCop-42-4 | L-PBF | 329.5 | 329.7 | 327.4 | 324.2 | 319.6 | 314.2 | 307.9 | 297.5 | - | - | - |
| GRCop-42-5 | L-PBF | 328.2 | 327.7 | 324.9 | 321.8 | 317.2 | 311.9 | 305.7 | 295.4 | - | - | - |
| GRCop-42-6 | L-PBF | 325.6 | 322.5 | 319.4 | 315.7 | 311.2 | 305.5 | 297.9 | 288.5 | - | - | - |
| GRCop-42-7 | L-PBF | 342.6 | 341.6 | 340.2 | 337.1 | 332.4 | 327.3 | 321.4 | 310.5 | - | - | - |
| GRCop-84-1 | L-PBF | 308.5 | 304.8 | 303.3 | 300.5 | 296.6 | 292.3 | 285.8 | 275.3 | - | - | - |
| GRCop-84-2 | L-PBF | 291.4 | 288.5 | 287.5 | 285.2 | 281.6 | 277.2 | 271.4 | 262.1 | - | - | - |

**Table 3.** Weight percentage of elements in the tested GRCop alloys [40].

| Element | GRCop-42-1 | GRCop-42-2 | GRCop-42-3 | GRCop-42-4 | GRCop-42-5 | GRCop-42-6 | GRCop-42-7 | GRCop-42-8 | GRCop-84-1 | GRCop-84-2 |
|---|---|---|---|---|---|---|---|---|---|---|
| Ag | 0.01 | <0.01 | <0.01 | <0.01 | <0.01 | <0.01 | <0.01 | <0.01 | <0.01 | <0.01 |
| Al | 0.06 | 0.06 | 0.06 | 0.06 | 0.06 | 0.07 | 0.04 | 0.06 | 0.01 | 0.03 |
| Co | 0.01 | <0.01 | <0.01 | <0.01 | <0.01 | <0.01 | <0.01 | <0.01 | <0.01 | <0.01 |
| Cr | 3.25 | 3.30 | 3.29 | 3.37 | 3.26 | 3.28 | 3.28 | 3.38 | 6.61 | 6.59 |
| Fe | 0.01 | <0.01 | <0.01 | <0.01 | 0.01 | <0.01 | <0.01 | <0.01 | <0.01 | <0.01 |
| Nb | 2.65 | 2.82 | 2.77 | 2.81 | 2.65 | 2.92 | 2.73 | 2.92 | 5.68 | 5.47 |
| Ni | 0.03 | <0.01 | <0.01 | 0.01 | 0.02 | <0.01 | 0.01 | <0.01 | <0.01 | <0.01 |
| O | 0.08 | 0.05 | 0.04 | 0.06 | 0.1 | 0.05 | 0.08 | 0.05 | 0.13 | 0.12 |
| P | <0.005 | <0.005 | <0.005 | <0.005 | <0.005 | <0.005 | <0.005 | <0.005 | <0.005 | 0.011 |
| Si | 0.02 | 0.01 | <0.01 | 0.03 | 0.04 | 0.01 | <0.01 | 0.02 | <0.01 | <0.01 |

### *2.2. Feature Selection and Analysis*

The independent features used in this work are the corresponding compositions of alloys, testing temperatures, and the target feature is thermal conductivity. The compositional features listed in the dataset consist of atomic percentage of elements Ni, Cu, Fe, Cr, Mo, Nb, Ta, Mn, Si, Co, Al, Ti, Zr, W, V, C, B, P, S, and La for each alloy.

A selection process filtered the features based on the statistical calculation of correlation between the independent variables. It was necessary to eliminate the features which were strongly correlated with each other since correlated features would lead to either overfit or underfit of the ML model. Pearson correlation coefficient statistical method was adopted to calculate the correlation between each pair of features [41]. A correlation value between two features approaching a +1 or −1 represents a strong correlation between them. To eliminate the highly correlated features, correlation values over the range of ±0.9 will be removed from the dataset. There was no need to calculate the correlation between the dependent feature with independent features since a higher correlation between them is required by the model to increase the model accuracy.

### 2.3. ML Methods

After feature selection, the TC dataset was applied for training and testing with machine learning regression models, including random forest regression (RFR), gradient boosting regression (GBR), Extreme Gradient Boosting (XGB) regression, Lasso regression (LR), and Ridge regression with default parameter setting. These methods have been successfully applied in several material science research projects for predicting physical properties of materials [18–25,42–44]. The 10-fold cross-validation approach [45] was used to evaluate the model performance and hyper-parameter tunning was performed to find the best parameter for better performance. For the accuracy of the results, it is very crucial to evaluate the predictions of all regression models to select the optimal one among them. For regression problems, two widely used metrics to evaluate the ML model's performance are absolute error (MAE) and root-mean-squared error (RMSE). Meanwhile, the R-Squared ($R^2$) is also used to evaluate ML models, since it helps to evaluate how much variance of the target property was captured by the regression model. Additionally, the mean square error (MSE) of each model is also calculated because it helps to compare the overall performance of ML models and verify whether the model is good at predicting alloy thermal conductivity accurately. In this work, all four metrics were used to evaluate the regression model performance and the mathematical formula is shown in Equations (2)–(5) [46]. The workflow of this ML method explained above is shown in Figure 2.

$$\mathrm{MAE} = \frac{1}{n}\sum_{i=1}^{n}|m_i - \hat{m}_i| \tag{2}$$

$$\mathrm{RMSE} = \sqrt{\frac{\sum_{i=1}^{n}(m_i - \hat{m}_i)^2}{n}} \tag{3}$$

$$R^2 = 1 - \frac{\sum_{i=1}^{n}(m_i - \hat{m}_i)^2}{\sum_{i=1}^{n}(m_i - \overline{m})^2} \tag{4}$$

$$\mathrm{MSE} = \frac{1}{n}\sum_{i=1}^{n}(m_i - \hat{m}_i)^2 \tag{5}$$

where $m_i$, $\hat{m}_i$, $\overline{m}$, and $n$ represents the experimental TC, ML predicted TC, mean of thermal conductivity, and sample size, respectively.

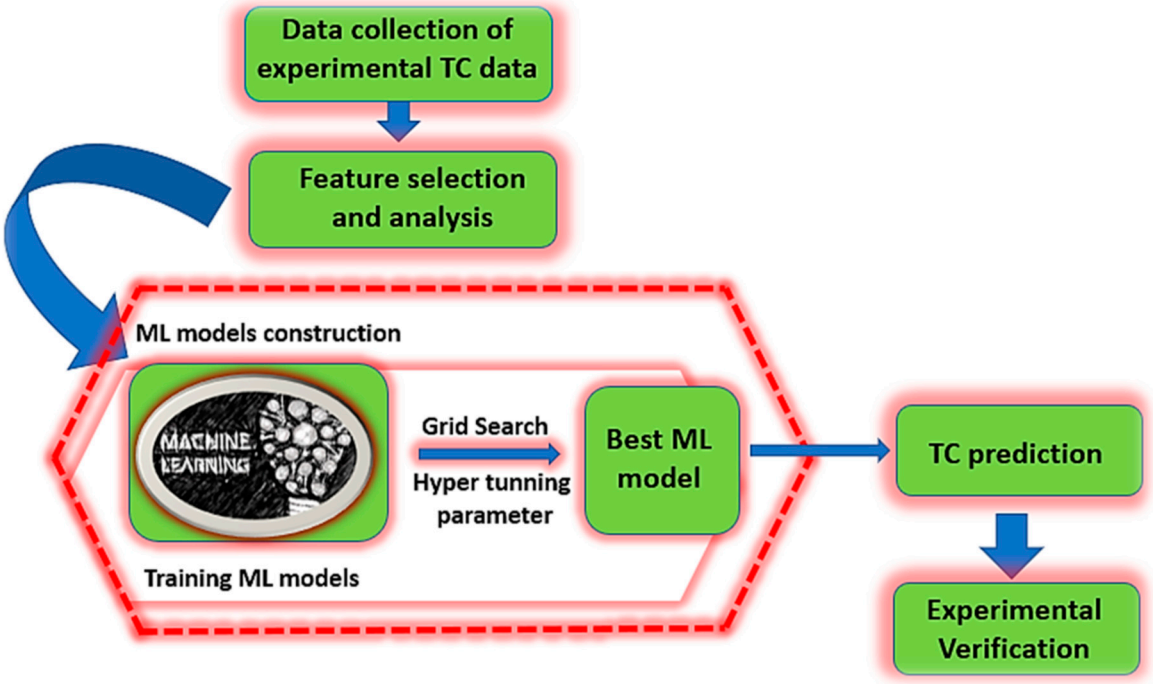


**Figure 2.** Schematic diagram of the workflow of overall procedure used in current work.

## 3. Results and Discussion

### *3.1. ML Models and Evaluation*

The correlation plot is shown in Figure 3 using a heat map. Among 21 independent features, elements Cr and Ni have the highest positive correlation of 0.5. The initial threshold of feature correlation was set to be ±0.9, which is a value frequently used in computing a correlation matrix. It is found that none of the initial features are highly correlated as all values of Pearson correlation lie below the initial threshold. This means all features are safe to use in the ML model.

It was found that three machine learning models had similar $R^2$ scores for both the training and testing dataset, as shown in Table 4. However, the remaining two models (ridge and lasso) train $R^2$ scores were similar but the test $R^2$ scores were relatively lower than those of the RF, GBR and XGB models. To differentiate which ML model is appropriate for the TC dataset, additional metrics such as RMSE, MAE, and MSE of each model are evaluated and compared. Five ML models and their metrics during training and testing data are shown in Figure 4. ML models with low MAE, MSE, and RMSE scores are better at making more accurate predictions. The MAE score of both Ridge and Lasso models are higher than RF, GBR, and XGB models, which indicates their low performance in the prediction of TC of the AM alloys dataset. The training RMSE of the RF model is higher than that of the GBR and XGB models. Meanwhile, the testing RMSE and MAE score of the GBR model is slightly higher than that of the XGB model. The MSE score of the XGB model is lower than that of all four ML models, indicating that the XGB model is better at predicting the TC of AM alloys. Analyzing the overall bargraph results in Figure 4a,b, the XGB model is found to have the best performance among all tested models with low RMSE and MAE scores and it was chosen as the best performing model for the TC prediction of AM alloys. The XGB model performs better than GBR because the XGB model uses a regularization technique which is incorporated in the XGB model for preventing the overfitting of the model [47]. The XGB model has more space for hyper tunning the parameters and computational method for tree pruning, which can reduce the noisy data present in a small dataset.

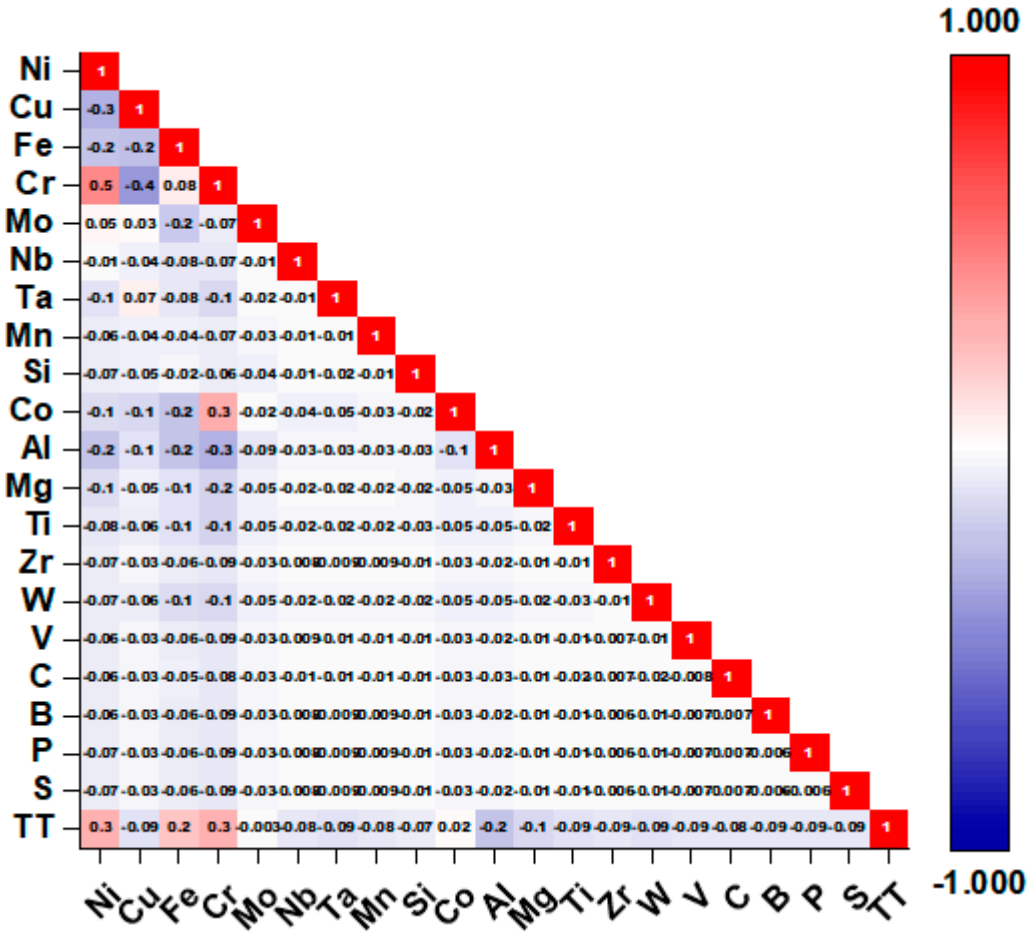


**Figure 3.** Pearson correlation heat map of all initial input independent features.

**Table 4.** Different ML models statistical summary $R^2$ for train and test data.

| ML Model | Train $R^2$ Score | Test $R^2$ Score |
|---|---|---|
| RF | 0.9997 | 0.9228 |
| GBR | 0.9997 | 0.9086 |
| XGB | 0.9999 | 0.9618 |
| Ridge | 0.9948 | 0.6953 |
| Lasso | 0.9956 | 0.7023 |

To improve the XGB model's prediction accuracy, the grid search method [48] was applied to find the best hyperparameters. Grid search builds a model for all combinations of hyperparameters and provides the best-tuned hyperparameters. Table 5 shows the list of tuned hyperparameters. By using the tuned parameter, the final XGB ML model is constructed. The scatter plot of training and testing data of TC predicted by XGB against the experimental work is shown in Figure 5a. The blue solid diagonal line on the plot represents the situation in which the predicted TC of alloys by the ML model match the experimental TC values, and in this case, the training and testing data points will lie along the blue line. According to Figure 5a, scatter plot of all the training and testing data points lie near the straight diagonal blue line indicating less error in prediction. However, a few testing data points have some higher variance, showing a lack of data around that range. In the future, more experimental data are expected to be added to improve the model. The K fold cross-validation test on the XGB model is also performed to identify any possible overfitting. The average 10-fold cross-validation score of the XGB model is found to be 99%. Based on a small TC dataset (294 datapoints), this score is very good.

Similar cross-validation results were found in the previous publication that consists of low data while predicting material properties [49,50]. For example, Huang et al. [49] found a 10-fold validation score of 0.91 while predicting the hardness of high entropy alloys from 85 experimentally collected hardness data. Huang et al. [50] found the average accuracy of support vector machine model in predicting single-phase, intermetallic phase and mixed phase of HEAs to be 86.3%, 91.2%, and 73.2%, respectively, using 4-fold cross validation. To verify the validity of the XGB model's prediction capability, the Ni-based Inconel 718-L-PBF superalloy (Ni-Cr-Mo-Nb) elemental composition and testing temperatures data are inserted in the XGB model, which were not present in the training and test dataset and were never seen by the model previously. Figure 5b shows the TC of Inconel 718 alloy at different temperatures predicted by the XGB model and the TC obtained experimentally. The consistency of TC of Inconel 718-L-PBF predicted by the XGB model with experiments further confirms the reliability of the model. The average mean error in predicting the TC of Inconel 718-L-PBF at different temperatures is 3.9%.

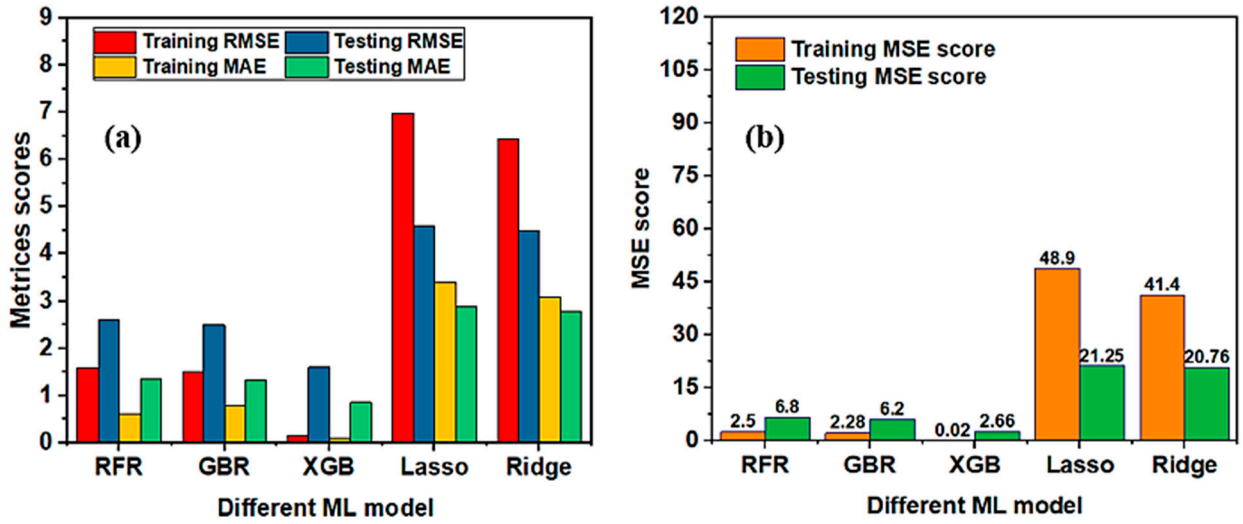


**Figure 4.** Evaluation of ML models using a variety of metrics. (**a**) RMSE and MAE for training and testing datasets, (**b**) computed MAE for training and testing datasets.

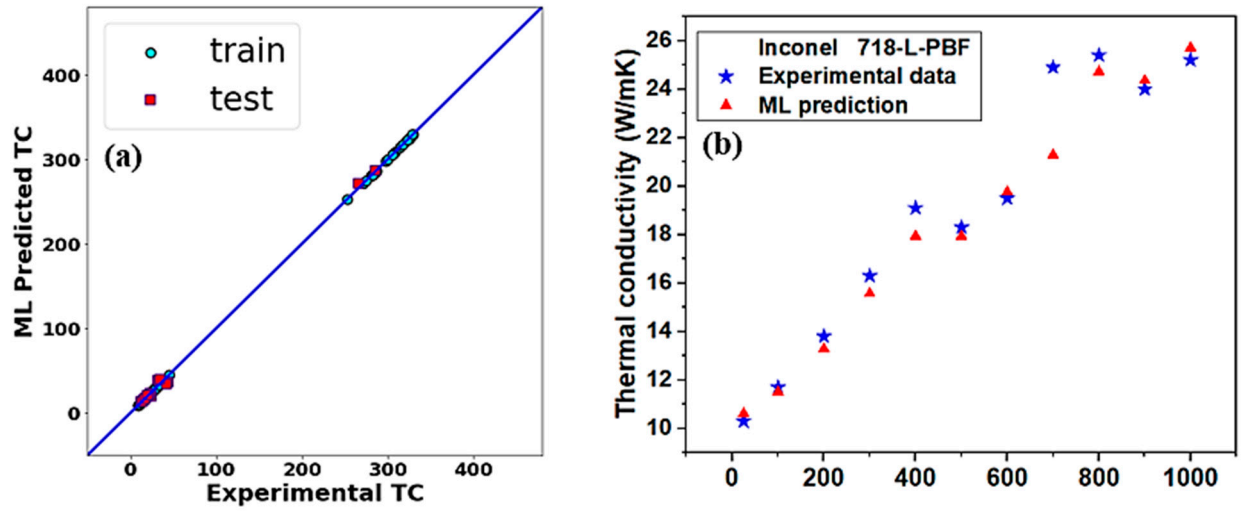


**Figure 5.** (**a**) The ML predicted TC as a function of the experimental TC for the training and testing dataset (**b**) TC of Inconel 718-L-PBF alloy predicted by ML and experiments at different temperatures (°C).

**Table 5.** Parameter, hyperparameter, and tuned hyperparameter obtained from Grid Search method.

| Parameters | Hyperparameter Value | Tuned Hyperparameter |
|---|---|---|
| Learning rate | [0.01, 0.1, 0.5] | 0.1 |
| max_depth | [3, 4, 5, 6, 8] | 6 |
| n_estimators | [100, 500, 900] | 900 |
| Subsample | [0.5, 0.7, 1.0] | 0.5 |
| Colsample_bytree | [0.3, 0.4, 0.6] | 0.4 |
| Gamma | [0, 1, 4] | 0 |

### *3.2. Additional Testing of the XGB Model*

To evaluate the reliability of the XGB model, further testing was conducted using a small dataset of GRCop alloys. These alloys have higher TC than the Ni- based superalloys and are created for high thermal conductivity applications such as electronics and aerospace sectors. The optimal XGB model was again trained with a 72-sample GRCop-alloy dataset to see how this model performs when the dataset is small. Since the number of datasets was reduced, the chances of finding the tuned hyperparameter for accurate ML model is challenging. For small datasets, it is found that the Bayesian optimization (BO) approach of hyperparameter tunning is more favorable than grid search [51,52]. This is due to Bayesian hyperparameter tuning working based on a probabilistic model, which searches for the best hyperparameter more effectively with lower computational costs. The advantage of Bayesian hyperparameter tunning is that it can search the optimal hyperparameter space and enhances the robustness of the ML models even with a small dataset. At first, the B0 approach will try to find out the initial set of hyperparameters from different combinations of hyperparameters based on the problem space and some presumptions regarding the potential effects of the model's hyperparameters. After finalizing the initial hyperparameters, BO uses a probabilistic model to construct a surrogate model which helps to estimate the performance of the model across a wide range hyperparameter space. The model is then trained using an initial set of hyperparameters. This process of training the model and evaluating model performance with different hyperparameter will help BO to collect more data points and makes the surrogate model more powerful and accurate. As the surrogate model improved, the algorithm will be more accurate in making an informed decision about where to search for the best hyperparameter. This process will help to find out the best hyperparameter from the limited dataset where the model is likely to have a better performance. Therefore, BO was employed to tune the XGB model hyperparameters. Table 6 lists the hyperparameters, their related search spaces, and the tuned hyperparameters for an XGB ML model that were discovered via Bayesian optimization. The hyperparameter max_depth was tuned from an integer of 1 to 6 which helps to regulate the maximum depth of each tree of the XGB model. It was found that the tuned hyperparameter for maximum depth was 4.16. The search space for the learning rate was from 0.01 to 0.4 and the tuned parameter was found to be 0.4 based on the BO approach. Similarly, the other hyperparameters such as n_estimators, subsample, colsample_by tree, min_child_weight, and gamma parameters are effectively tuned and adjusted using BO to improve the model's performance on the small dataset.

**Table 6.** The hyperparameter, space searching, and tuned hyperparameter based on the BO method.

| Hyperparameter | Space Searching | Tuned Hyperparameter |
|---|---|---|
| max_depth | (1, 6) | 4.16 |
| learning_rate | (0.01, 0.4), | 0.4 |
| n_estimators | (100, 700), | 448.06 |
| subsample | (0.1, 1), | 0.1 |
| colsample_bytree | (0.1, 1), | 1 |
| min_child_weight | (1, 4), | 1.0 |
| gamma | (0, 4) | 0 |

The XGB model was trained and tested on the small dataset of GRCop alloys (Cu-Cr-Nb) using the tuned hyperparameters from BO. The tuned XGB model had an R2 score of 0.995, RMSE of 0.847, and MAE of 0.723, demonstrating excellent performance on the test data. In order to evaluate how well the tuned XGB model performed, a completely new set of GRCop alloy data (GRCop-42-8) with composition and testing temperatures is supplied to the model for prediction. The thermal conductivity predicted using the XGB model is shown in Table 7. The predicted TC using the XGB model is consistent with the experimental result, demonstrating that the model had correctly generalized the unseen data with slight changes in the elements. Figure 6 and Table 7 show the TC of GRCop-42-8 alloy predicted using the ML XGB model, together with experimental results, at different temperatures. It is found that ML XGB model prediction and experimental results show a similar trend with a total average prediction error of 2.08%. It implies that selecting the best hyperparameter can significantly impact the ML model's prediction accuracy, rather than the number of datasets. However, the larger dataset can provide more information for the model, but careful selection of the hyperparameters has a significant impact on model accuracy. Therefore, the trained XGB model shows a promising possibility that it could be utilized in predicting the thermal conductivity of new composition alloys with high accuracy. The trained ML model proposed by Yanjing et al. [53] has a mean absolute error (MAE) of 0.39 W/mK and a coefficient of determination (R2) while predicting the TC of crystal materials. Similarly, Wang et al. [54] applied four different ML models to compute the TC of crystal materials and found that the XGBoost model has the best prediction accuracy based on R2 and MAE scores. The MAE and R2 of the XGBoost model were 0.95 and 0.96, respectively. The MAE and R2 of the model on the testing set were 2.13 W/mK and 0.90, respectively. The XGB model in this work on the training set has MAE and R2 values of 0.10 W/mK and 0.99, respectively. On the testing set, the MAE and R2 of the XGB model were 0.86 W/mK and 0.96, respectively, which suggests that it has strong generalizability.

**Table 7.** Comparison of thermal conductivity (TC) experimentally measured and predicted by ML model for a new GRCop alloy.

| Testing Temperature (°C) | Experimental TC (W/mK) | TC Predicted Using XGB Model (W/mK) | Error % |
|---|---|---|---|
| 25 | 338.536 | 330.21 | 2.45 |
| 100 | 336.187 | 329.21 | 2.08 |
| 200 | 333.851 | 326.96 | 2.06 |
| 300 | 330.246 | 323.96 | 1.9 |
| 400 | 325.17 | 318.39 | 2.08 |
| 500 | 319.44 | 313.58 | 1.83 |
| 600 | 312.59 | 305.27 | 2.34 |
| 700 | 302.2228 | 296.31 | 1.95 |

To find the relationship between the features applied to construct the GBR model and TC, SHAP (SHapley Additive exPlanations) [55] is used to plot the feature importance. The SHAP method takes the mean absolute value of each feature from the entire dataset to generate the feature importance plot which is shown in Figure 7. There is no physical relationship between feature importance and the TC of materials. The feature importance is only ranked based on the scores of each independent feature during the training of the model. It was found that the composition of Ni holds the most important feature, which denotes it has the highest score among other features and is very helpful in predicting thermal conductivity. The interesting thing to note here was that the statistical mean value of the Ni element holds 35% in the training dataset and due to its high presence, it may have the highest SHAP value. The other six important features in predicting the TC are the composition of Cu, Si, Fe, C, Ti, and the testing temperature. It was found from the previous study that the alloying of elements influenced the thermal conductivity of alloys [56–59]. For instance, the F82H steel has low TC and the addition of copper and tungsten improves

its thermal conductivity [60]. Many studies show that the thermal conductivity decreases when the test temperature increases for pure metals, for example, Cu [61] Al [62], Au [63], Ag [64], and so forth. However, this is not the case for alloys over the test temperature range in this study, whose thermal conductivity value generally increases as test temperature rises. Defects, especially point defects like solid solutions commonly existing in alloys with a high content of alloying elements, show a strong scattering effect on electrons, which raise thermal resistance and most likely lead to different temperature-dependence features of thermal-physical properties. It appears that the SHAP model was able to find the physical connection between the TC and the composition of elements. Therefore, the SHAP model will be further examined for providing guidance for AM alloy design in future.

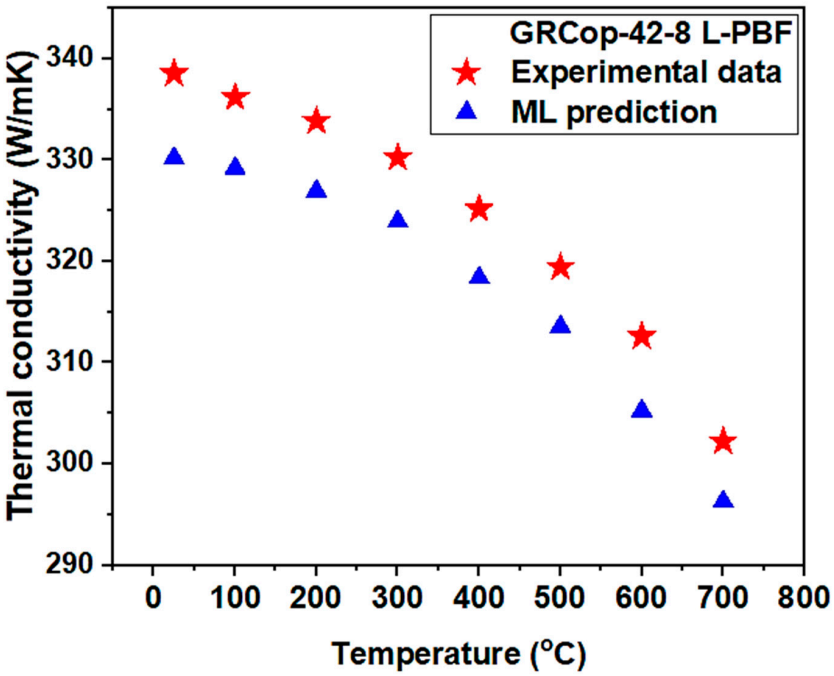


**Figure 6.** TC of GRCop-42-8 alloy predicted via the ML XGB model and experiments at different temperatures.

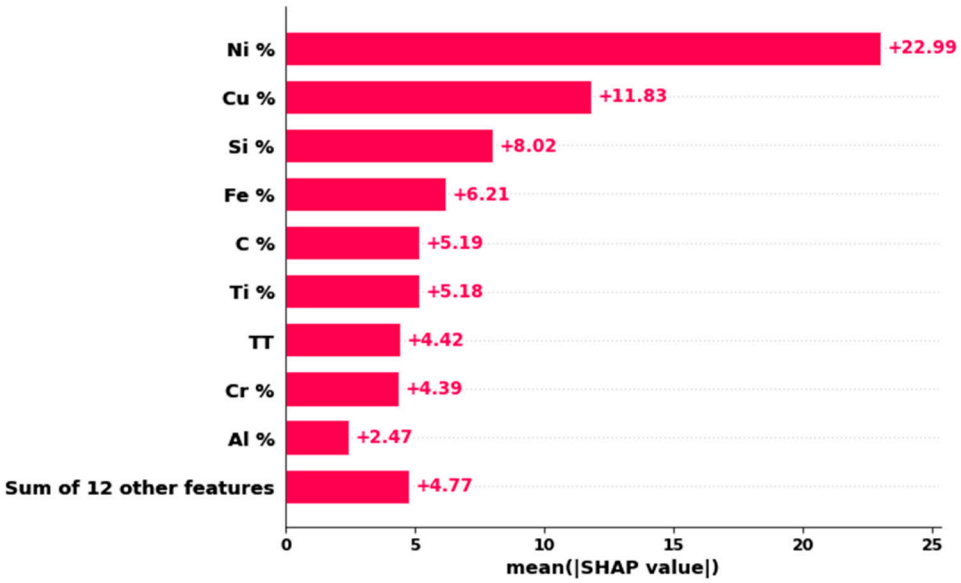


**Figure 7.** Ranking of important features using the SHAP method.

## 4. Conclusions

In this work, different ML models were used to predict and experimentally validate the thermal conductivity of different additively manufactured alloys. Based on the metrics used to evaluate the performance of all models, the XGB ML model was found to be promising in predicting the thermal conductivity of alloys. The TC of alloy prediction is based on the composition of elements and testing temperature and does not require additional theoretical calculations and experimental setups. This method is faster, more economical, and more precise than many other physics-based simulations. The predictions made by the XGB model for AM alloy L-PBF Inconel 718 and L-PBF GRCop-42 are consistent with the experimentally measured values. The R2, MAE, RMSE and MSE of the XGB model were 0.96, 0.86 W/mK, 1.63 W/mK and 2.66 W/mK, respectively. The SHAP method shows that the composition of Ni, Cu, Si, Fe, and C holds the most importance in predicting the thermal conductivity of alloys. This current ML method could be utilized in screening various newly developed compositions of AM alloys to search for the potential alloy of the desired thermal conductivity. This model will continue to be refined with additional TC measurements of alloys from various families and it will be used to optimize the elemental composition of AM alloys to improve the TC. The model performance of the XGB model can be improved by carefully selecting, adding more data, and optimizing the input features or learning algorithms. In the future, physics-based models can be developed to calculate the relevant properties of alloys, and can be further applied to machine learning for optimization until the best composition with the desired TC is found.

**Author Contributions:** Conceptualization, S.G. and C.Z.; methodology, C.Z., S.E., Y.C., U.B. and H.D.; software, C.Z., Y.C. and H.D.; validation, S.G., P.R.G. and C.Z.; formal analysis, C.Z., H.D. and Y.C.; investigation, C.Z., H.D., U.B. and Y.C.; resources, S.G. and P.R.G.; data curation, C.Z., H.D. and Y.C.; writing—original draft preparation, U.B.; writing—review and editing, S.G., C.G and P.R.G.; visualization, C.Z.; supervision, S.G.; project administration, S.G.; funding acquisition, S.G. and P.R.G.; All authors have read and agreed to the published version of the manuscript.

**Funding:** This work was supported by the US National Science Foundation under Grant OIA-1946231 and Louisiana Board of Regents for the Louisiana Materials Design Alliance (LAMDA). The experimental data generation is partially supported by the National Aeronautics and Space Administration (NASA)'s Established Program to Stimulate Competitive Research (EPSCoR) grant number 80NSSC19M0149 and NSF #OIA-2118756.

**Data Availability Statement:** The data and code that support the findings of this study are available at GitHub (https://github.com/uttambhandari91/TC_calculation (accessed on 1 September 2023)).

**Conflicts of Interest:** The authors declare no conflict of interest.

## References

1. Dong, Z.Q.; Wang, J.G.; Guan, Z.P.; Ma, P.K.; Zhao, P.; Li, Z.J.; Lu, T.S.; Yan, R.F. Effect of short T6 heat treatment on the thermal conductivity and mechanical properties of different casting processes Al-Si-Mg-Cu Alloys. *Metals* **2021**, *11*, 1450.
2. Li, S.; Yang, X.; Hou, J.; Du, W.J. A review on thermal conductivity of magnesium and its alloys. *J. Magnes. Alloys* **2020**, *8*, 78–90.
3. Zhang, C.; Du, Y.; Liu, S.; Liu, Y.; Sundman, B.J.T.A. Thermal conductivity of Al–Cu–Mg–Si alloys: Experimental measurement and CALPHAD modeling. *Thermochim. Acta* **2016**, *635*, 8–16.
4. Blakey-Milner, B.; Gradl, P.; Snedden, G.; Brooks, M.; Pitot, J.; Lopez, E.; Leary, M.; Berto, F.; Du Plessis, A. Metal additive manufacturing in aerospace. *Mater. Des.* **2021**, *209*, 110008.
5. Niknam, S.A.; Mortazavi, M.; Li, D. Additively manufactured heat exchangers: A review on opportunities and challenges. *Int. J. Adv. Manuf. Technol.* **2021**, *112*, 601–618.
6. Pan, H.; Pan, F.; Yang, R.; Peng, J.; Zhao, C.; She, J.; Gao, Z.; Tang, A. Thermal and electrical conductivity of binary magnesium alloys. *J. Mater. Sci.* **2014**, *49*, 3107–3124.
7. Miura, A.; Osada, T.; Kawagishi, K.; Uchida, K.I. Thermal transport properties of Ni–Co-based superalloy. *AIP Adv.* **2020**, *10*, 125118.
8. Cheng, H.H.; Huang, D.S.; Lin, M.T. Heat dissipation design and analysis of high power LED array using the finite element method. *Microelectron. Reliab.* **2012**, *52*, 905–911.
9. Li, W.; Mingo, N.; Lindsay, L.; Broido, D.A.; Stewart, D.A.; Katcho, N.A. Thermal conductivity of diamond nanowires from first principles. *Phys. Rev. B* **2012**, *85*, 195436.

10. Ward, A.; Broido, D.; Stewart, D.A.; Deinzer, G. Ab initio theory of the lattice thermal conductivity in diamond. *Phys. Rev. B* **2009**, *80*, 125203.
11. Shiomi, J.; Esfarjani, K.; Chen, G. Thermal conductivity of half-Heusler compounds from first-principles calculations. *Phys. Rev. B* **2011**, *84*, 104302.
12. Broido, D.A.; Malorny, M.; Birner, G.; Mingo, N.; Stewart, D.A. Intrinsic lattice thermal conductivity of semiconductors from first principles. *Appl. Phys. Lett.* **2007**, *91*, 231922.
13. Ward, A.; Broido, D.A. Intrinsic phonon relaxation times from first-principles studies of the thermal conductivities of Si and Ge. *Phys. Rev. B* **2010**, *81*, 085205.
14. Esfarjani, K.; Chen, G.; Stokes, H.T. Heat transport in silicon from first-principles calculations. *Phys. Rev. B* **2011**, *84*, 085204.
15. Eliassen, S.N.; Katre, A.; Madsen, G.K.; Persson, C.; Løvvik, O.M.; Berland, K. Lattice thermal conductivity of TixZr yHf1− x− y NiSn half-Heusler alloys calculated from first principles: Key role of nature of phonon modes. *Phys. Rev. B* **2017**, *95*, 045202.
16. Ding, G.; Gao, G.Y.; Yao, K.L. Examining the thermal conductivity of the half-Heusler alloy TiNiSn by first-principles calculations. *J. Phys. D Appl. Phys.* **2015**, *48*, 235302.
17. Lampin, E.; Palla, P.L.; Francioso, P.A.; Cleri, F. Thermal conductivity from approach-to-equilibrium molecular dynamics. *J. Appl. Phys.* **2013**, *114*, 033525.
18. Liu, X.; Zhang, J.; Pei, Z. Machine learning for high-entropy alloys: Progress, challenges and opportunities. *Prog. Mater. Sci.* **2022**, *131*, 101018.
19. Zhou, Z.; Zhou, Y.; He, Q.; Ding, Z.; Li, F.; Yang, Y. Machine learning guided appraisal and exploration of phase design for high entropy alloys. *Npj. Comput. Mater.* **2019**, *5*, 128.
20. Zhou, Y.; Srinivasan, P.; Körmann, F.; Grabowski, B.; Smith, R.; Goddard, P.; Duff, A.I. Thermodynamics up to the melting point in a TaVCrW high entropy alloy: Systematic abinitio study aided by machine learning potentials. *Phys. Rev. B* **2022**, *105*, 214302.
21. Schleder, G.R.; Padilha, A.C.; Acosta, C.M.; Costa, M.; Fazzio, A. From DFT to machine learning: Recent approaches to materials science—A review. *J. Phys. Mater.* **2019**, *2*, 032001.
22. Schmidt, J.; Marques, M.R.; Botti, S.; Marques, M.A. Recent advances and applications of machine learning in solid-state materials science. *Npj. Comput. Mater.* **2019**, *5*, 83.
23. Butler, K.T.; Davies, D.W.; Cartwright, H.; Isayev, O.; Walsh, A. Machine learning for molecular and materials science. *Nature* **2018**, *559*, 547–555.
24. Raccuglia, P.; Elbert, K.C.; Adler, P.D.; Falk, C.; Wenny, M.B.; Mollo, A.; Zeller, M.; Friedler, S.A.; Schrier, J.; Norquist, A.J. Machine-learning-assisted materials discovery using failed experiments. *Nature* **2016**, *533*, 73–76.
25. Chen, L.; Tran, H.; Batra, R.; Kim, C.; Ramprasad, R. Machine learning models for the lattice thermal conductivity prediction of inorganic materials. *Comput. Mater. Sci.* **2019**, *170*, 109155. [CrossRef]
26. Jaafreh, R.; Kang, Y.S.; Hamad, K. Interfaces. Lattice thermal conductivity: An accelerated discovery guided by machine learning. *ACS Appl. Mater Interfaces* **2021**, *13*, 57204–57213. [CrossRef] [PubMed]
27. Mortazavi, B.; Podryabinkin, E.V.; Roche, S.; Rabczuk, T.; Zhuang, X.; Shapeev, A.V. Machine-learning interatomic potentials enable first-principles multiscale modeling of lattice thermal conductivity in graphene/borophene heterostructures. *Mater. Horiz.* **2020**, *7*, 2359–2367. [CrossRef]
28. Tewari, A.; Dixit, S.; Sahni, N.; Bordas, S.P. Machine learning approaches to identify and design low thermal conductivity oxides for thermoelectric applications. *Data-Centric Eng.* **2020**, *1*, e8. [CrossRef]
29. Miyazaki, H.; Tamura, T.; Mikami, M.; Watanabe, K.; Ide, N.; Ozkendir, O.M.; Nishino, Y. Machine learning based prediction of lattice thermal conductivity for half-Heusler compounds using atomic information. *Sci. Rep.* **2021**, *11*, 13410. [CrossRef] [PubMed]
30. Wu, S.; Kondo, Y.; Kakimoto, M.A.; Yang, B.; Yamada, H.; Kuwajima, I.; Lambard, G.; Hongo, K.; Xu, Y.; Shiomi, J.; et al. Machine-learning-assisted discovery of polymers with high thermal conductivity using a molecular design algorithm. *Npj. Comput. Mater.* **2019**, *5*, 66. [CrossRef]
31. Gradl, P.; Tinker, D.C.; Park, A.; Mireles, O.R.; Garcia, M.; Wilkerson, R.; Mckinney, C.J. Performance. Robust metal additive manufacturing process selection and development for aerospace components. *J. Mater. Eng. Perform.* **2022**, *31*, 6013–6044. [CrossRef]
32. Gradl, P.R.; Mireles, O.R.; Protz, C.S.; Garcia, C.P. *Metal Additive Manufacturing for Propulsion Applications*; Timothy, C., Lieuwen, T.C., Eds.; American Institute of Aeronautics and Astronautics, Inc.: Reston, VA, USA, 2022.
33. Zeng, C.; Guo, S.; Gradl, P.R.; Belcher, T. Thermophysical Properties of Select AM Alloys. In *Metal Additive Manufacturing for Propulsion Applications*; Progress in Astronautics and Aeronautics; American Institute of Aeronautics and Astronautics, Inc.: Reston, VA, USA, 2022; pp. 775–824.
34. Joseph, J.; Hodgson, P.; Jarvis, T.; Wu, X.; Stanford, N.; Fabijanic, D.M. Effect of hot isostatic pressing on the microstructure and mechanical properties of additive manufactured AlxCoCrFeNi high entropy alloys. *Mater. Sci. Eng. A* **2018**, *733*, 59–70. [CrossRef]
35. Hafenstein, S.; Werner, E. Pressure dependence of age-hardenability of aluminum cast alloys and coarsening of precipitates during hot isostatic pressing. *Mater. Sci. Eng. A* **2019**, *757*, 62–69. [CrossRef]
36. Lario, J.; Vicente, Á.; Amigó, V.J.M. Evolution of the microstructure and mechanical properties of a Ti35Nb2Sn alloy post-processed by hot isostatic pressing for biomedical applications. *Mater. Sci. Eng. A* **2021**, *11*, 1027. [CrossRef]

37. Xu, Z.; Zhang, Y. Quench rates in air, water, and liquid nitrogen, and inference of temperature in volcanic eruption columns. *Earth Planet. Sci. Lett.* **2002**, *200*, 315–330. [CrossRef]
38. Nishibata, T.; Kojima, N. Effect of quenching rate on hardness and microstructure of hot-stamped steel. *J. Alloys Compd.* **2013**, *577*, S549–S554. [CrossRef]
39. Zeng, C.; Zhang, B.; Hemmasian Ettefagh, A.; Wen, H.; Yao, H.; Meng, W.J.; Guo, S. Mechanical, thermal, and corrosion properties of Cu-10Sn alloy prepared by laser-powder-bed-fusion additive manufacturing. *Addit. Manuf.* **2020**, *35*, 101411. [CrossRef]
40. Chen, Y.; Zeng, C.; Ding., H.; Emanet, S.; Gradl, P.R.; Ellis, D.L.; Guo, S. Thermophysical properties of additively manufactured (AM) GRCOP-42 and GRCOP-84. *Mater. Today Commun.* **2023**, *36*, 106665. [CrossRef]
41. Rodgers, J.L.; Nicewander, W.A. Thirteen ways to look at the correlation coefficient. *Am. Stat.* **1988**, *42*, 59–66. [CrossRef]
42. Yang, C.; Ren, C.; Jia, Y.; Wang, G.; Li, M.; Lu, W. A machine learning-based alloy design system to facilitate the rational design of high entropy alloys with enhanced hardness. *Acta Mater.* **2022**, *222*, 117431. [CrossRef]
43. Khakurel, H.; Taufique, M.; Roy, A.; Balasubramanian, G.; Ouyang, G.; Cui, J.; Johnson, D.D.; Devanathan, R. Machine learning assisted prediction of the Young's modulus of compositionally complex alloys. *Sci. Rep.* **2021**, *11*, 17149. [CrossRef]
44. Yang, K.; Xu, X.; Yang, B.; Cook, B.; Ramos, H.; Krishnan, N.; Smedskjaer, M.M.; Hoover, C.; Bauchy, M. Predicting the Young's modulus of silicate glasses using high-throughput molecular dynamics simulations and machine learning. *Sci. Rep.* **2019**, *9*, 8739. [CrossRef] [PubMed]
45. Jung, Y. Multiple predicting K-fold cross-validation for model selection. *J. Nonparametr. Stat.* **2018**, *30*, 197–215. [CrossRef]
46. Pedregosa, F.; Varoquaux, G.; Gramfort, A.; Michel, V.; Thirion, B.; Grisel, O.; Duchesnay, É. Scikit-learn: Machine learning in Python. *J. Mach. Learn. Res.* **2011**, *12*, 2825–2830.
47. Chen, T.; Guestrin, C. Xgboost: A scalable tree boosting system. In Proceedings of the 22nd ACM SIGKDD International Conference on Knowledge Discovery and Data Mining, San Francisco, CA, USA, 13–17 August 2016.
48. LaValle, S.M.; Branicky, M.S.; Lindemann, S.R. On the relationship between classical grid search and probabilistic roadmaps. *Int. J. Robot. Res.* **2004**, *23*, 673–692. [CrossRef]
49. Huang, X.; Jin, C.; Zhang, C.; Zhang, H.; Fu, H. Machine learning assisted modelling and design of solid solution hardened high entropy alloys. *Mater. Des.* **2021**, *211*, 110177. [CrossRef]
50. Huang, W.; Martin, P.; Zhuang, H.L. Machine-learning phase prediction of high-entropy alloys. *Acta Mater.* **2019**, *169*, 225–236. [CrossRef]
51. Lee, S.Y.; Byeon, S.; Kim, H.S.; Jin, H.; Lee, S. Deep learning-based phase prediction of high-entropy alloys: Optimization, generation, and explanation. *Mater. Des.* **2021**, *197*, 109260. [CrossRef]
52. Snoek, J.; Larochelle, H.; Adams, R.P. Practical bayesian optimization of machine learning algorithms. *Adv. Neural Inf. Process.* **2012**, *25*, 1–9.
53. Sun, Y.; Hu, W. Novel machine learning framework for thermal conductivity prediction by crystal graph convolution embedded ensemble. *SmartMat* **2022**, *3*, 474–481. [CrossRef]
54. Wang, X.; Zeng, S.; Wang, Z.; Ni, J. Identification of crystalline materials with ultra-low thermal conductivity based on machine learning study. *J. Phys. Chem. C* **2020**, *124*, 8488–8495. [CrossRef]
55. Lundberg, S.M.; Lee, S.-I. A unified approach to interpreting model predictions. *Adv. Neural Inf. Process.* **2017**, *30*, 4768–4777.
56. Wang, G.; Li, Y. Effects of alloying elements and temperature on thermal conductivity of ferrite. *J. Appl. Phys.* **2019**, *126*, 125118. [CrossRef]
57. Chen, L.; Lü, S.; Guo, W.; Li, J.; Wu, S. High thermal conductivity of highly alloyed Mg-Zn-Cu alloy and its mechanism. *J. Alloys Compd.* **2022**, *918*, 165614. [CrossRef]
58. Choi, S.W.; Kim, Y.M.; Kim, Y.C.; Kang, C.S. Technology. Effects of alloying elements on mechanical and thermal characteristics of Al-6wt-% Si-0.4 wt-% Mg–(Cu) foundry alloys. *Mater. Sci. Technol.* **2019**, *35*, 1365–1371. [CrossRef]
59. Qin, R.; Yan, R.F.; Guan, Z.P.; Zhang, G.Q.; Song, J.W.; Ren, M.W.; Wang, J.G. Effect of vanadium on Fe-rich phase, mechanical properties and thermal conductivity of hypoeutectic Al–Si alloy. *Mater. Res. Express.* **2021**, *8*, 026518. [CrossRef]
60. Heo, J.; Hashimoto, N.; Oka, H.; Noto, H. Improvement of thermal conductivity by adding tungsten and/or copper wire in F82H. *J. Nucl. Sci. Technol.* **2022**, *59*, 216–221. [CrossRef]
61. Moore, J.; McElroy, D.; Graves, R.S. Thermal conductivity and electrical resistivity of high-purity copper from 78 to 400 K. *Can. J. Phys.* **1967**, *45*, 3849–3865. [CrossRef]
62. Brandt, R.; Neuer, G. Electrical resistivity and thermal conductivity of pure aluminum and aluminum alloys up to and above the melting temperature. *Int. J. Thermophys.* **2007**, *28*, 1429–1446. [CrossRef]
63. Ho, C.Y.; Powell, R.W.; Liley, P.E. Thermal conductivity of the elements: A comprehensive review. *J. Phys. Chem. Ref. Data* **1974**, *1*, 11974.
64. Tritt, T.M. *Thermal Conductivity: Theory, Properties, and Applications*; Springer Science & Business Media: New York, NY, USA, 2005.